The Wave-Coherent Stress and Turbulent Structure over Swell Waves

ZHONGSHUI ZOU,[a] JINBAO SONG,[b] FANGLI QIAO,[c] DONGXIAO WANG,[a] AND JUN A. ZHANG[d,e]

[a] *School of Marine Sciences, Sun Yat-Sen University, Southern Marine Science and Engineering Guangdong Laboratory (Zhuhai), Zhuhai, China*
[b] *Ocean College, Zhejiang University, Zhoushan, China*
[c] *First Institute of Oceanography, Ministry of Natural Resources, and Laboratory for Regional Oceanography and Numerical Modeling, Qingdao National Laboratory for Marine Science and Technology, Qingdao, China*
[d] *NOAA/AOML/HRD, Miami, Florida*
[e] *Cooperative Institute for Marine and Atmospheric Studies, University of Miami, Miami, Florida*

(Manuscript received 26 July 2023, in final form 1 June 2024, accepted 6 June 2024)

ABSTRACT: The generation of ocean surface waves by wind has been studied for a century, giving rise to wave forecasting and other crucial applications. However, the reacting force of swell waves on the turbulence in the marine atmospheric boundary layer (ABL) remains unknown partly due to the unclear magnitude and profile of wave-coherent (WC) stress. In this study, the intersection frequency between the energy-containing range and inertial subrange range in the turbulent spectra is identified based on the attached eddy model (AEM), as the intersection modulated by swell wave could help to comprehend the physical process between the ocean surface wave and the marine ABL. Using observations from a fixed platform located in the South China Sea, this study shows that the intersection when the WC stress accounts for a lower proportion of the total wind stress (<10%) follows $U/(2\pi z)$ given by AEM, where U is the wind speed and z is the height. While the intersection depends on the drag coefficient of WC stress for the case, WC stress accounts for a large part of the total wind stress (>10%). Considering the unclear magnitude and profile of WC stress, this study derives a new function to depict the WC stress.

SIGNIFICANCE STATEMENT: Turbulence located in the energy-containing range of the spectra is the primary source of momentum, heat, and water vapor fluxes between the ocean and marine atmospheric boundary layer (ABL). Thus, a better understanding of the turbulent structure within the wave boundary layer can help us accurately parameterize those fluxes. In addition to absorbing energy from the marine ABL, waves, especially swell waves, influence the turbulent structure. However, until now, the turbulent structure is unclear due to the unclear wave-coherent stress size and profile. In this study, a function that can depict the wave-coherent stress is proposed. We found that the wave-coherent stress can modulate the intersection between the energy-containing range and the inertial subrange range in the turbulent spectra.

KEYWORDS: Turbulence; Oceanic waves; Wind stress; Sea state; Surface fluxes

1. Introduction

Wind and surface waves are strongly coupled. One of the interests about their couple is the momentum flux transport by turbulence, as it plays a decisive role in the dynamic processes in the lower atmosphere and upper ocean. Under the force of the wind, the generation of surface waves drew lots of attention, and after 100 years of study, the wave forecast became available by ignoring the reacting force of waves on the marine atmospheric boundary layer (ABL). However, when wind waves propagate thousands of kilometers and become swell, they affect marine ABL turbulence.

The turbulence modulated by swell concerns two different categories, i.e., the ocean surface waves and turbulence. To make this study easy to understand, this paper introduces the current understanding of the reacting force of waves on the marine ABL and the turbulent theory recently developed on laboratory and rigid land surface first. Then, the object of this study is given.

a. The reacting force of waves on the marine ABL

The mechanism of how surface waves are generated by wind has been a research topic of interest since the beginning of the twentieth century when Jeffreys first assumed that wind was sheltered by waves, leading to a pressure difference [also named the wave-coherent (WC) pressure] between the windward and leeward sides (Jeffreys 1925). After the invalidation of Jeffreys' sheltering theory demonstrated by laboratory measurements on solid waves (Janssen 2004), two theories, one that is based on the resonance mechanism proposed by Phillips (1957) and the other that is based on the shear instability proposed by Miles (1957), making the wave forecast become available.

The WC pressure in the lower part of the marine ABL is the key to the growth of surface waves. In addition to absorbing energy from the air, the WC pressure could excite WC perturbation in the marine ABL. Correspondingly, the lower part of the marine ABL, where the WC perturbations begin to support momentum exchange, is the wave boundary layer (WBL, https://indd.adobe.com/view/1ca38c75-9f87-435e-9391-343c88d24c32). Within the WBL, the total momentum flux or the total wind stress can be separated into the WC stress and

Corresponding author: Jinbao Song, songjb@zju.edu.cn

DOI: 10.1175/JPO-D-23-0144.1

turbulent stress as follows (Grachev and Fairall 2001; Grachev et al. 2003):

$$\boldsymbol{\tau} = \boldsymbol{\tau}_{\text{wave}} + \boldsymbol{\tau}_{\text{turb}}, \tag{1.1}$$

where $\boldsymbol{\tau} = -\rho_a(\overline{wu}\mathbf{i} + \overline{wv}\mathbf{j})$, $\boldsymbol{\tau}_{\text{wave}} = -\rho_a(\overline{\tilde{w}\tilde{u}}\mathbf{i} + \overline{\tilde{w}\tilde{v}}\mathbf{j})$ is the WC stress, $\boldsymbol{\tau}_{\text{turb}} = -\rho_a(\overline{w'u'}\mathbf{i} + \overline{w'v'}\mathbf{j})$ is the turbulent stress, and $\mathbf{i}$ and $\mathbf{j}$ represent the longitudinal and lateral unit vectors, respectively. The tilde (~) represents the WC perturbation and the prime (′) represents the turbulence generated by the wind shear and buoyance force.

The study of the influence of the WC perturbation on the marine ABL originates from Harris, who first reported wave-driven wind in a wave tank experiment in 1966 (Harris 1966). Further field observations showed that WC perturbations significantly affect the magnitude and direction of wind stress. For example, Donelan et al. (1997) showed that the presence of old waves makes the drag coefficient different from that of young waves. By separating the wind stress in the high-, middle-, and low-frequency bands, Rieder and Smith (1998) showed that the WC perturbation was concentrated in the middle band and that the stress carried by the WC perturbation makes the total stress off the mean wind direction. The modulation of wind stress by WC stress was further confirmed by Grachev et al. (2003). Högström et al. (2015) reviewed several experiments and found that the WC stress observed in the Tropical Ocean Global Atmosphere (TOGA) Coupled Ocean–Atmosphere Response Experiment (COARE), the Rough Evaporation Duct (RED) experiment, and San Clemente Ocean Probing Experiment (SCOPE) could make the total wind stress higher than that predicted by COARE 3.0 while Baltic Sea Swell Experiment (BASE) observed lower total wind stress than COARE 3.0. Recently, Grare et al. (2013b) also observed lower total wind stress.

The effect of WC stress on marine ABL has drawn much attention since the negative wind gradient under swell conditions was reported by Rutgersson et al. (2001). To explicitly illustrate the interaction between the swell and marine ABL, several models have been developed to describe the upward WC stress, including the direct numerical simulation (DNS; Sullivan et al. 2000; Kihara et al. 2007) and large-eddy simulation (LES; Sullivan et al. 2008; Rutgersson et al. 2012; Sullivan et al. 2014; Jiang et al. 2016) and one-dimensional models (Hanley and Belcher 2008; Semedo et al. 2009; Song et al. 2015; Zou et al. 2018). Those studies showed that the upward WC stress leads to a strong wind gradient near the surface by following a layer of a nearly constant or negative wind profile above, as reported by Grachev and Fairall (2001) and Smedman et al. (2009). However, the wind profile is on the other hand for the young wave when it absorbs energy from marine ABL, i.e., the downward WC stress can lead to a gentler wind gradient than Monin–Obukhov similarity theory (MOST) within the WBL (Babanin et al. 2018).

The WC stress is a key parameter in studying the effect of swell on the wind stress and the wind profile. However, the magnitude and the profile of WC stress are still unclear. Most current studies (Makin et al. 1995; Hanley and Belcher 2008; Semedo et al. 2009; Cifuentes-Lorenzen et al. 2018; Babanin et al. 2018; Zou et al. 2018; Wu and Qiao 2022) assumed the WC stress decays exponentially with height. This exponential decay format of WC stress differs from shear instability, which gives a constant value below the height where wind speed and wave phase speed are equal. It is also different from laboratory experiments by Buckley and Veron (2016) and LES by Cao and Shen (2021).

b. The turbulent structure in the ABL

The marine ABL is a complicated system containing WC perturbation, wind shear, and buoyancy-force-generated turbulence. To study the effect of swell waves on the wind stress and the wind profile, the turbulent structure should be understood as turbulence carries the momentum flux and affects the wind gradient. Before that, the turbulent characteristics without waves are introduced in the section.

Since much attention has been given to the turbulent structure in the inertial subrange, Perry and Chong (1982), Perry et al. (1986), Marušić and Perry (1995), and Perry and Marušić (1995) developed the attached eddy model (AEM) based on Townsend (1976)'s wall-attached eddy hypothesis. Through dimensional analysis and overlap argument, Perry et al. showed that the overlap of outer and inner scaled flows leads to a k^{-1} power law.

In contrast to the turbulent eddies, which are located in the inertial subrange and behave as a $k^{-5/3}$ power law in turbulent spectra, the k^{-1} power law corresponds to the mean energy-containing eddies and leads to the gradient of the wind profile. Extensive studies over the laboratory or over land (Katul and Chu 1998; Kunkel and Marusic 2006; Del Álamo and Jiménez 2009; Hutchins et al. 2012; Katul et al. 2012; Pan and Chamecki 2016; Wang et al. 2021b) have shown that even though the ABL easily suffers from changes in the weather, nonuniform terrain, and buoyancy, similar to the turbulence within the laboratory, the horizontal velocity spectra in the near-neutral ABL follow the AEM.

For the vertical velocity spectra, however, the observations over land showed some contradictions compared with the AEM. For example, Ghannam et al. (2018) showed that their three experiments depict a remarkable k^{-1} power law, while the others do not. To illustrate the different behaviors of vertical turbulence structures, Drobinski et al. (2004) explained that the nonexistence of the k^{-1} law in vertical velocity spectra was due to the dampening effect of the surface based on rapid distortion theory (Townsend 1976). As a result, the vertical velocity spectra in the shear surface layer (the intermediate sublayer of ABL) show the k^{-1} power law but not in the eddy surface layer (the low part of ABL).

In addition to the AEM, the k^{-1} power law can also be derived based on the "top-down model" proposed by Hunt and Morrison (2000) and Hunt and Carlotti (2001). By combining the k^{+0} power law shown in the low wavenumber (Högström et al. 2002), the horizontal spectra in the ABL can be obtained as follows:

$$E_{uu} \propto \begin{cases} k^{-5/3}, & k \geq a_{uu} z^{-1} \\ k^{-1}, & b_{uu}\Lambda^{-1} \leq k < a_{uu} z^{-1} \\ k^{+0}, & k < b_{uu}\Lambda^{-1} \end{cases}. \tag{1.2}$$

Moreover, the vertical spectra can be obtained as follows:

$$E_{ww} \propto \begin{cases} k^{-5/3}, & k \geq a_{ww} z^{-1} \\ k^{-1}, & b_{ww}\Lambda^{-1} \leq k < a_{ww} z^{-1} \\ k^{+0}, & k < b_{ww}\Lambda^{-1} \end{cases}, \tag{1.3}$$

where Λ is the length scale of the largest eddy, which has an order of magnitude similar to the boundary layer thickness, and the coefficients a and b are constants of $O(1)$. Notably, within the eddy surface layer $b_{ww}\Lambda^{-1} = a_{ww}z^{-1}$, the k^{-1} law does not exist in the vertical spectra according to rapid distortion theory.

With the growth of computing power, many works have focused on this process using LES and DNS in recent years, for example, Drobinski et al. (2007) demonstrated its existence in ABL using LES. However, few researchers have considered the turbulent structure modulated by waves, except for Wang et al. (2021a) showed that waves can reconstruct the attached eddies, and Hao and Shen (2022) showed a decayed response of the turbulence fluctuations over waves due to impulsive wind speed changes.

Huang et al. (2021) and Liu et al. (2022) recently studied the attached eddies over ocean surface waves. They showed that although the turbulence has a remarkable k^{-1} (or f^{-1}) power law, the intersection between the energy-containing range and inertial subrange, i.e., the values of a_{ii} (here, $i = u$ or w) in Eqs. (1.2) and (1.3), depends on the terrain characteristic. For wind blowing over a swell, Liu et al. (2022) suggested that the intersection should consider the wave phased speed. While for wind following swell when the swell exerted upward momentum flux, they explained that the larger values of a_{uu} and a_{ww} are due to the WC pressure. However, to the best of our knowledge, no researcher has explored the attached eddies over swell waves when the swell waves absorb energy from the marine ABL.

c. Object of this study

The WBL is the primary place where atmospheric energy and oceanic energy are exchanged. For the research community, the accurate parameterization of the total momentum flux carried by turbulence can significantly influence the accuracy of atmospheric and oceanic circulation models, wave development models, and climate models (Janssen and Viterbo 1996). Phillips (1957) and Miles (1957) have made forecasts of short wind waves available. However, for long swell waves, their interaction with the marine ABL turbulence remains unclear. As the eddies satisfying the k^{-1} power law most efficiently transfer momentum flux, this study uses three levels of observations at a fixed platform to study its intersection with the $k^{-5/3}$ power law modulated by WC stress. Considering the controversial method of WC stress description, a new function is derived in this study. This paper is different from that of Grare et al. (2018) who provided a function to describe WC perturbations; we focused on the WC stress.

This paper is organized as follows. In section 2, observations and the analytic method are presented. In section 3, the results are shown. In section 4, a discussion is presented. Finally, conclusions are provided in section 5.

2. Experimental and analytic methods

a. Observations

The data used in this study were collected from a fixed platform. The platform is located in the South China Sea and is positioned ~6 km from the shore. The body of the platform is a hollow steel structure anchored by three huge concrete tanks on the seafloor. The water depth around the platform is ~16 m deep. Figure 1 shows the location and structure of the platform.

During the measurement period of 17 March–14 May 2018, Chen et al. (2020) observed the turbulent wind velocity at heights of 8.4, 12.4, and 15.3 m above the mean ocean level by using three ultrasonic anemometers (Campbell CPEC310) at a sampling rate of 10 Hz. Below the ultrasonic anemometers, an ADCP (Nortek Signature 1000) was used to observe the surface elevations every hour. The sampling rate of the ADCP was 4 Hz, and each wave measurement lasted 1024 s. The horizontal distance between the ADCP and ultrasonic anemometers was approximately 55 m.

b. Data and analytic method

To increase reliability, the raw continuous observation data were separated into half-hour runs, and each run was subjected to quality control procedures, including spike removal and tilt correction (Zou et al. 2017).

The nonstationary (or mesoscale) motions in the ABL have the potential to affect the turbulent structure, violate similarity theory, and contaminate the flux (Vickers and Mahrt 2003); thus, not all data passing quality control are used. The nonstationary can be checked by using the Ogive curve. The Ogive curve is defined as the cumulative integral of the cospectrum from high to low frequencies:

$$\mathbf{O_g}(f) = \mathrm{Og}_x\mathbf{i} + \mathrm{Og}_y\mathbf{j} = \int_{f_{\max}}^{f} \mathrm{Co}_{uw}(f)df\mathbf{i} + \int_{f_{\max}}^{f} \mathrm{Co}_{vw}(f)df\mathbf{j}, \tag{2.1}$$

where Co is the cospectra and $f_{\max}$ is the maximum frequency of the cospectra. If the run contains nonstationary motions, the Ogive curve will not increase monotonically with decreasing frequency. For runs containing nonstationary motions, if their Ogive curves fluctuate severely at frequencies larger than $\sim 10^{-2}$ Hz, those runs are rejected. However, if the nonstationary motions have low frequencies ($<\sim 10^{-2}$ Hz), the flux carried by those motions is removed when computing the total flux. As a result, the total wind stress computed from 10-Hz wind turbulent data is $|\int_{f_{\max}}^{f_{\min}} \mathrm{Co}_{uw}(f)df\mathbf{i} + \int_{f_{\max}}^{f_{\min}} \mathrm{Co}_{vw}(f)df\mathbf{j}|$, where $f_{\min}$ is the frequency where nonstationary motions occur.

Figure 2 shows the time series of several variables during the observation after quality control. Figure 2a shows that most wind speeds ranged from 1 to 8 m s^{-1}, and the wind blew from the east (~90°). The significant wave height was not very high, ranging from 0.6 to 1.5 m, with most of the wave propagating from the east–southeast (~120°, Fig. 2b). Figure 2c shows the atmospheric stability z/L and wave age

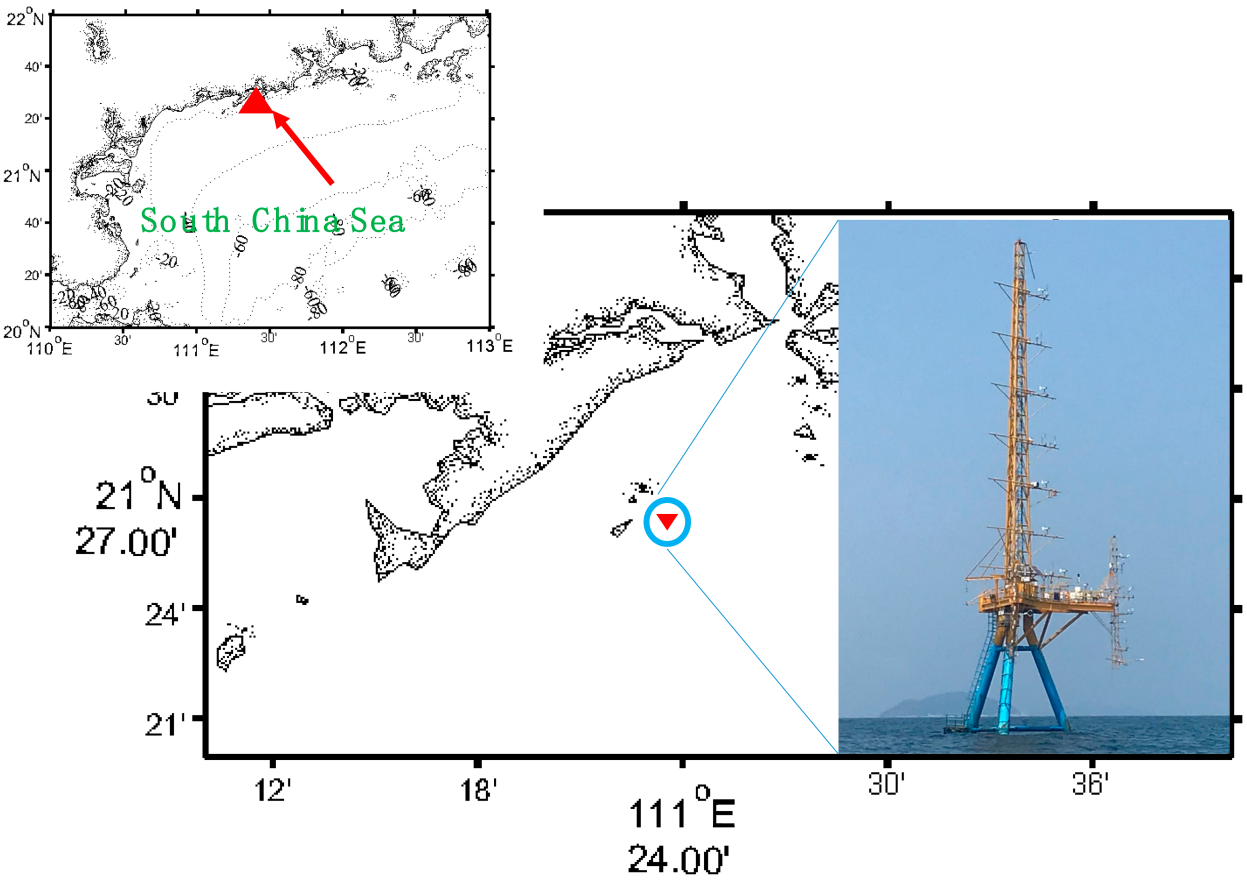

FIG. 1. Position of the platform within the South China Sea and photograph of the platform. The red arrow points to the location of the platform. The upper-left picture shows the topography of the South China Sea.

computed by using the observation at 8.4 m above the mean ocean level, where $L = -u_*^3\theta_v/g\kappa\overline{w'\theta_v'}$. Most of the time, the atmosphere was unstable. The wave age is $c_p/U_{8.4}$, where c_p is the dominant peak wave phase speed. It can be seen that the ocean was dominated by swells ($c_p/U_{8.4} > 1.2$). By dividing the waves into wind waves and swell waves using the Wave Identification and Tracking System (Hanson and Jensen 2004), Fig. 2d shows the ratio of swell energy to wind-wave energy. The observation shows that 48% of the ratio is larger than 5.

To analyze the influence of swell waves on the turbulent structure, the height of the WBL should be defined to check whether the observations are within the WBL. Theoretically, studies (Chalikov and Makin 1991; Chalikov 1995) show that the height is proportional to the significant wave height and above several significant wave heights, the WC stress becomes 0. Using this method, the height of the WBL estimated by Cifuentes-Lorenzen et al. (2018) is 1–3 m. However, Ortiz-Suslow et al. (2021) observed a proportion of WC stress at 16 m. Considering that it does not have a conventional definition of WBL height, instead of determining the height of the WBL to check if the observation is within the WBL, the proportion of the WC stress to the total wind stress is computed in this study. Moreover, all runs are partitioned into two groups: one segment has a small portion of the WC stress compared with the total wind stress (<10%) and the WC stress of the other segment accounts for more than 10% of the total wind stress.

The method proposed by Grare et al. (2013a) is used to extract the WC perturbations and stress as follows:

$$S_{\tilde{u}\tilde{u}} = S_{uu}\gamma^2_{\tilde{\eta}u},$$

$$S_{\tilde{v}\tilde{v}} = S_{vv}\gamma^2_{\tilde{\eta}v}, \quad \text{and}$$

$$S_{\tilde{w}\tilde{w}} = S_{ww}\gamma^2_{\tilde{\eta}w}. \tag{2.2}$$

The WC stress can be obtained as follows:

$$\overline{\tilde{w}\tilde{u}} = \int \sqrt{S_{\tilde{u}\tilde{u}}S_{\tilde{w}\tilde{w}}}\cos(\theta_{\tilde{\eta}\tilde{u}} - \theta_{\tilde{\eta}\tilde{w}})df, \quad \text{and}$$

$$\overline{\tilde{w}\tilde{v}} = \int \sqrt{S_{\tilde{v}\tilde{v}}S_{\tilde{w}\tilde{w}}}\cos(\theta_{\tilde{\eta}\tilde{v}} - \theta_{\tilde{\eta}\tilde{w}})df, \tag{2.3}$$

where $\gamma^2_{\tilde{\eta}u} = |S_{\tilde{\eta}u}|^2/(S_{\tilde{\eta}\tilde{\eta}}S_{uu})$, $\gamma^2_{\tilde{\eta}v} = |S_{\tilde{\eta}v}|^2/(S_{\tilde{\eta}\tilde{\eta}}S_{vv})$, and $\gamma^2_{\tilde{\eta}w} = |S_{\tilde{\eta}w}|^2/(S_{\tilde{\eta}\tilde{\eta}}S_{ww})$ are the squared coherencies and $\theta_{\tilde{\eta}\tilde{u}} = \arg(S_{\tilde{\eta}u})$, $\theta_{\tilde{\eta}\tilde{v}} = \arg(S_{\tilde{\eta}v})$, and $\theta_{\tilde{\eta}\tilde{w}} = \arg(S_{\tilde{\eta}w})$ are the phase shifts between the wind fluctuations and wave elevations. This method requires observations with the same sampling rate; thus, all the high-frequency raw data were averaged

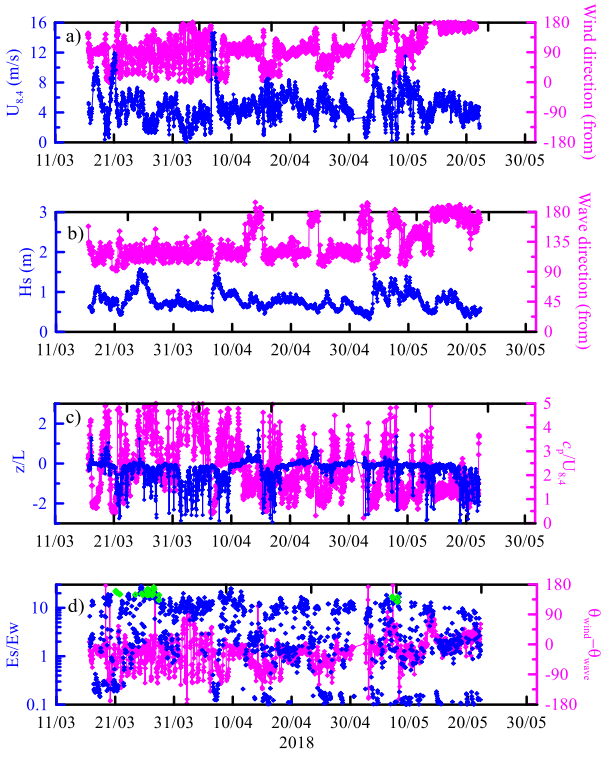

FIG. 2. Time series of the (a) wind speed and wind direction at 8.4 m above the mean ocean level, (b) significant wave height (Hs) and wave direction, (c) atmospheric stability and wave age, and (d) the ratio of swell energy to wind-wave energy and the angle difference between wave and wind. The green diamonds are the data when WC accounts for a large part of total wind stress. The horizontal ordinate shows the local time.

to 1 Hz when we computed WC perturbations and stress. The distance between two instruments is also taken into account when we compute the phase shift: $(\theta_{\tilde{\eta}\tilde{u},\tilde{\eta}\tilde{w}})_{\text{corrected}} = (\theta_{\tilde{\eta}\tilde{u},\tilde{\eta}\tilde{w}})_{\text{obs}} + (\Delta x/\lambda)$, where $(\theta_{\tilde{\eta}\tilde{u},\tilde{\eta}\tilde{w}})_{\text{corrected}}$ is the corrected phase shift and $(\theta_{\tilde{\eta}\tilde{u},\tilde{\eta}\tilde{w}})_{\text{obs}}$ is the phase shift computed from observation, Δx is the projection of the distance of two instruments on the direction of wave propagation, and λ is the wavelength.

To derive the WC stress by using Eqs. (2.2) and (2.3), the waves and wind should be simultaneously measured. The total number of runs in which the waves and wind were both measured is 1302, and 112 runs are selected to analyze whether their turbulent structures follow the AEM by computing the turbulent spectra. These runs have a steady wind speed that ranges from 5.61 to 12.7 m s^{-1} with directions ranging from 30° to 98°. Figure 1 shows that those winds blew from the land surface and the fetch ranged from 10 km to open sea. When the wind direction is <60°, the fetch is shorter than 26 km. Those winds may encounter an internal boundary layer (IBL). However, Huang et al. (2021) have analyzed the effect of limited fetch on wind profile and eliminated the IBL. The significant wave height ranged from 0.49 to 1.46 m, and the peak direction ranged from 44° to 160°. Due to the high wind speed and low significant wave height, the WC stress is small compared with the total wind stress (<10% of the total wind stress).

For the runs in which WC stress accounts for more than 10% of the total wind stress, 75 runs are selected (Fig. 3a). Those runs absorb energy from the wind and have narrow peak frequency, direction, and a larger ratio of swell energy to wind-wave energy (the green diamonds in Fig. 2d). As an example, Figure 3b shows one run of the directional wave spectrum. The significant wave height of those runs ranged from 0.52 to 1.57 m and had wind speeds ranging from 1.00 to 5.34 m s^{-1}. The wind direction is larger than 40° and the angle difference between the wind and the waves ranges from −53° to 7° (Fig. 2d). The wave steepness ranged from 0.019 to 0.071, much smaller than the wave breaking criteria given by Toffoli et al. (2010).

Figures 3c and 3d show the total wind stress and WC stress changing with wind speed at three levels. It can be seen that WC stress decreases with the height. The picture also shows that the total wind stress and WC stress roughly follow $|\boldsymbol{\tau}|(|\boldsymbol{\tau}_{\text{wave}}|) = aU^2 + b$. The coefficients a and b are given in Table 1. The correlation coefficient $[r^2 = \text{cov}(|\boldsymbol{\tau}_{\text{wave}}|/\rho_a, U^2)/\sigma(|\boldsymbol{\tau}_{\text{wave}}|/\rho_a)/\sigma(U^2)]$ between the three levels of total wind stress and the wind speed is 0.78. For WC stress, it is 0.79.

3. Results

a. *The f^{-1} power law in the spectra*

The AEM shows that under high Reynolds number, the k^{-1} region is formed by a cluster of hairpin vortices. Other than using the wavenumber-dependent turbulent spectra $E_{ii}(k)$, the frequency-dependent turbulent spectra $S_{ii}(f)$ were analyzed. These two forms of turbulent spectra can be transformed from each other based on Taylor's frozen hypothesis (Taylor 1938).

Figure 4 shows two runs of the turbulent spectra. Here, the premultiplied form $fS_{ii}(f)$ is given because if we multiply $S_{ii}(f)$ with f, the f^{-1} power law will appear as a plateau on a log–log scale that can be easily identified. To check the influence of the surface waves on turbulence, the wave spectra are also added to the bottom of each panel.

The observations show that when the WC stress accounts for a small proportion of the total wind stress (Figs. 4a–c), the pronounced plateaus in the horizontal turbulent spectra can extend to almost a decade in frequency, while the lengths of the plateaus in the vertical turbulent spectrum are short and decrease with a decreasing height (Hunt and Morrison 2000; Hunt and Carlotti 2001).

Compared with Figs. 4a–c, the lateral and vertical spectra, which contain a large proportion of WC stress (Figs. 4e,f), have remarkable peaks. The peaks are formed by WC perturbations and thus have the same frequency as the wave in the spectral peak. The peaks lead to very short plateaus, and the plateaus in Fig. 4f) are not even clearly visible.

Katul et al. (2012) showed that an eddy whose wavenumber k roughly equals $1/z$ separates the energy-containing range and inertial subrange. Based on Taylor's frozen hypothesis, their intersection frequency is $a_{ii}U/(2\pi z)$. To determine the intersection frequency in our observation, this study used $y_1 \sim f^{+0}$ and $y_2 \sim f^{-2/3}$ to fit $fS_{ii}(f)$. Here, the inertial

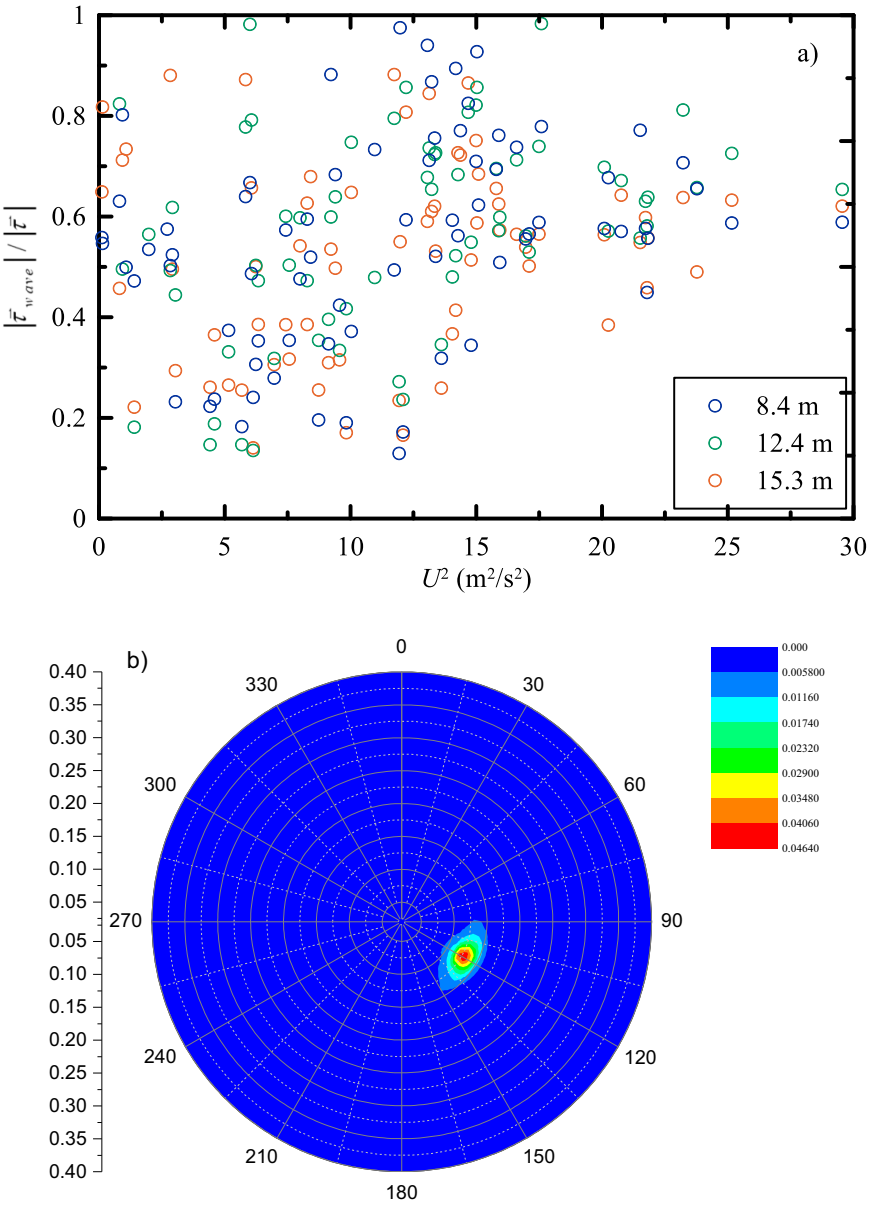

FIG. 3. (a) The ratio of WC stress to total wind stress changing with U^2. (b) An example of directional wave spectra. (c),(d) The total wind stress and WC stress changing with the wind speed. The blue, green, and brown circles represent the data at 8.4, 12.4, and 15.3 m above the mean ocean level, respectively. The solid, dash, and dash–dotted lines represent the relationship with $U^2 : |\boldsymbol{\tau}|(|\boldsymbol{\tau}_{\text{wave}}|) = aU^2 + b$ at 8.4, 12.4, and 15.3 m, respectively. The values of (a) and (b) are given in Table 1.

subrange is detected by using the algorithm for robust identification of the inertial subrange (ARIIS) given by Ortiz-Suslow et al. (2020), and the energy-containing range is detected by searching the premultiplied spectra at a frequency range less than the end frequency of the inertial subrange to find where the premultiplied spectra fit f^{+0} best. The intersection of two lines was the intersection frequency. For the turbulent spectra within the WBL, the same method was applied when they followed an apparent f^{-1} power law. When the turbulent spectra contain remarkable wave-related peaks, the upper and lower frequencies at which the wave-related peaks intersect with the turbulence spectra are determined. Then, their mean values were taken as the intersection frequency.

The intersection frequencies determined from the above method (vertical cyan lines) and those predicted from $U/(2\pi z)$ (vertical magenta lines) are plotted in Fig. 4. The result seems random, and it is difficult to determine if the observed intersection frequencies follow $U/(2\pi z)$ from one run.

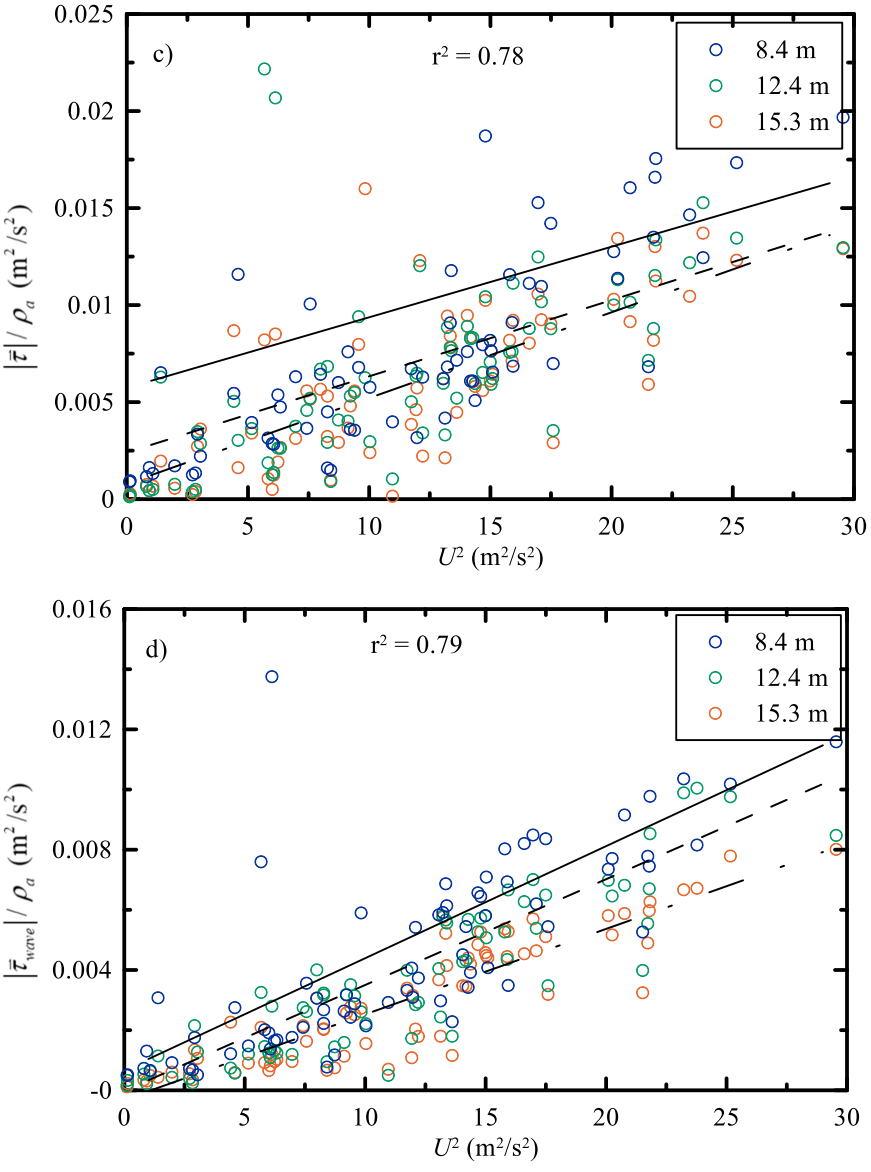

FIG. 3. (*Continued*)

Figures 5a–c show the statistics of the observed intersection frequencies changing with $U/(2\pi z)$. Here, the asterisks represent the intersection frequency in which the proportion of WC stress is small, and the circles represent the intersection frequency in which the proportion of WC stress is very large. The result shows that the asterisks roughly follow Katul et al. (2012)'s prediction: $f_i = a_{ii}U/2\pi z$, where $i = u$, v, or w represent the longitudinal, lateral, and vertical components, respectively; and a_{uu}, a_{vv}, and a_{ww} are equal to 1.15 ± 0.07, 2.80 ± 0.17, and 4.92 ± 0.31, respectively. The correlation coefficients between the observed intersection frequency f_{io} and $U/(2\pi z)$ are 0.75, 0.81, and 0.78 for the longitudinal, lateral, and vertical

TABLE 1. The coefficients a and b in $|\boldsymbol{\tau}|(|\boldsymbol{\tau}_{wave}|) = aU^2 + b$ with 1.96 standard error.

	$\lvert\boldsymbol{\tau}\rvert$			$\lvert\boldsymbol{\tau}_{wave}\rvert$		
	$a \times 10^{-3}$	$b \times 10^{-3}$	RMSE	$a \times 10^{-3}$	$b \times 10^{-3}$	RMSE
8.4 m	0.36 ± 0.34	5.73 ± 4.01	0.0092	0.37 ± 0.071	0.67 ± 0.85	0.0019
12.4 m	0.39 ± 0.26	2.42 ± 1.65	0.0037	0.35 ± 0.041	−0.038 ± 0.50	0.0011
15.3 m	0.44 ± 0.093	0.80 ± 1.23	0.0027	0.29 ± 0.032	−0.39 ± 0.42	0.0010

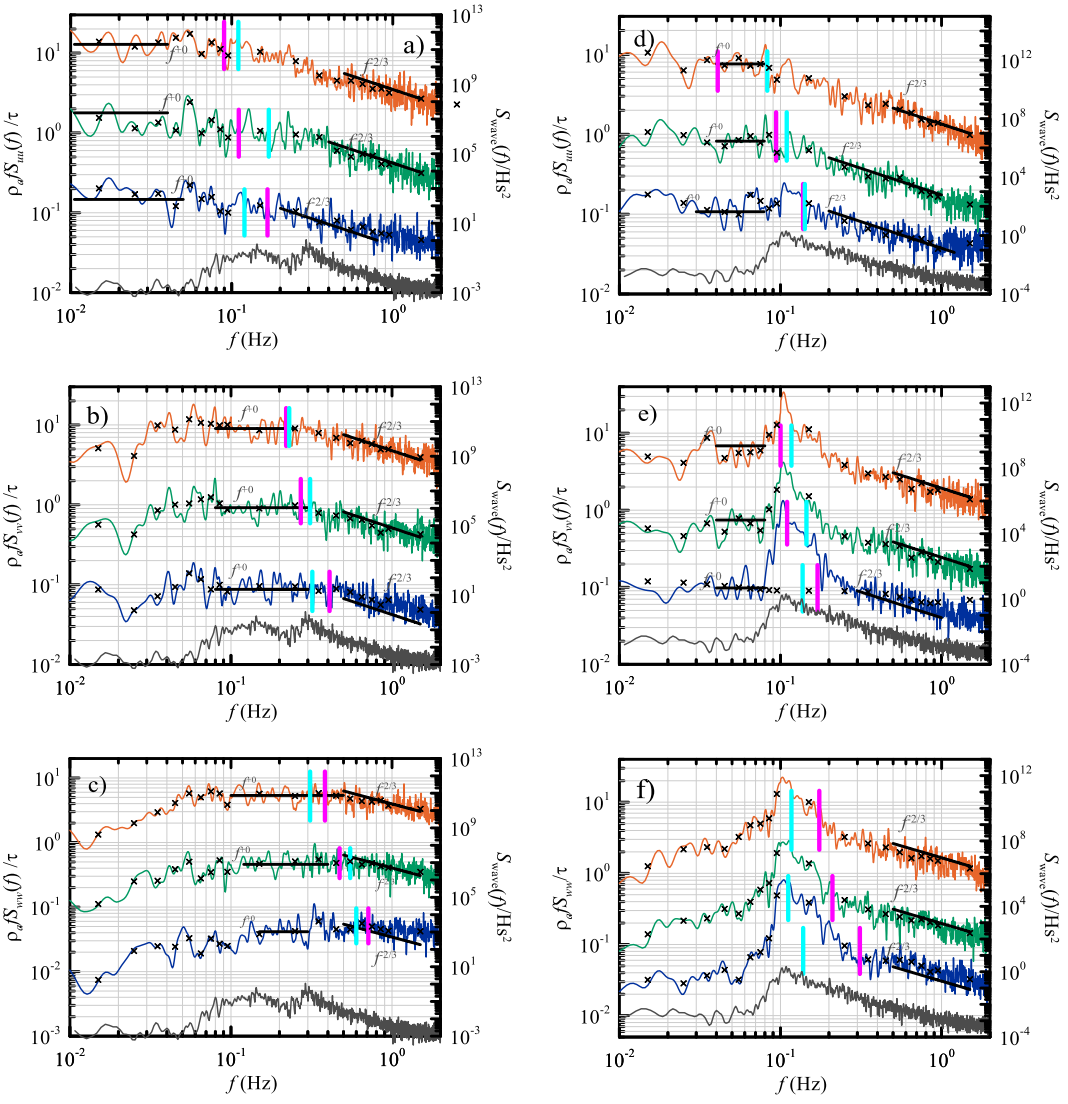

FIG. 4. Examples of (a) premultiplied longitudinal velocity spectra, (b) lateral velocity spectra, and (c) vertical velocity spectra when the WC stress accounts for a small proportion of the total wind stress. For a large proportion of WC stress, they are shown in (d)–(f). The crosses are the bin-averaged values. The spectra are normalized by the total momentum flux. To avoid the overlap of spectra, the normalized spectra at 8.4 m (blue lines) and 15.3 m (brown lines) are amplified by a factor of 1/10 and 10, respectively. The green lines represent the spectra at 12.4 m. The dark lines marked with f^0 and $f^{-2/3}$ can be used to determine the slopes of the spectra. The vertical magenta lines in all panels show the intersection frequency predicted by $U/(2\pi z)$, and the vertical cyan lines are the real intersection frequency. The dark lines at the bottom of each panel are normalized wave spectra.

components, respectively. The root-mean-square error (RMSE) between the observed intersection frequency and that determined from $U/2\pi z$ are 0.03, 0.06, and 0.12.

The behaviors of the circles are different from those of the asterisks: the intersection frequency in the longitudinal velocity spectra is higher than that predicted by $U/2\pi z$, while in the lateral and vertical spectra, they do not have a clear relationship with $U/(2\pi z)$. Their correlation coefficients are -0.29, -0.05, and -0.03 for the longitudinal, lateral, and vertical components, respectively.

The height and wind speed-dependent intersection frequencies, i.e., $U/(2\pi z)$, are obtained from rigid surfaces. It may be inappropriate to describe the intersection frequencies when there is a large proportion of WC stress. Thus, we infer that not only the height and wind speed but also the WC pressure could affect the intersection frequency.

The effects of the height, wind speed, and WC stress are presented in Fig. 6. Figure 6 shows the ratio of $U/(2\pi z)$ to the observed intersection frequency changing with the wind speed and WC stress using the circle data in Fig. 5.

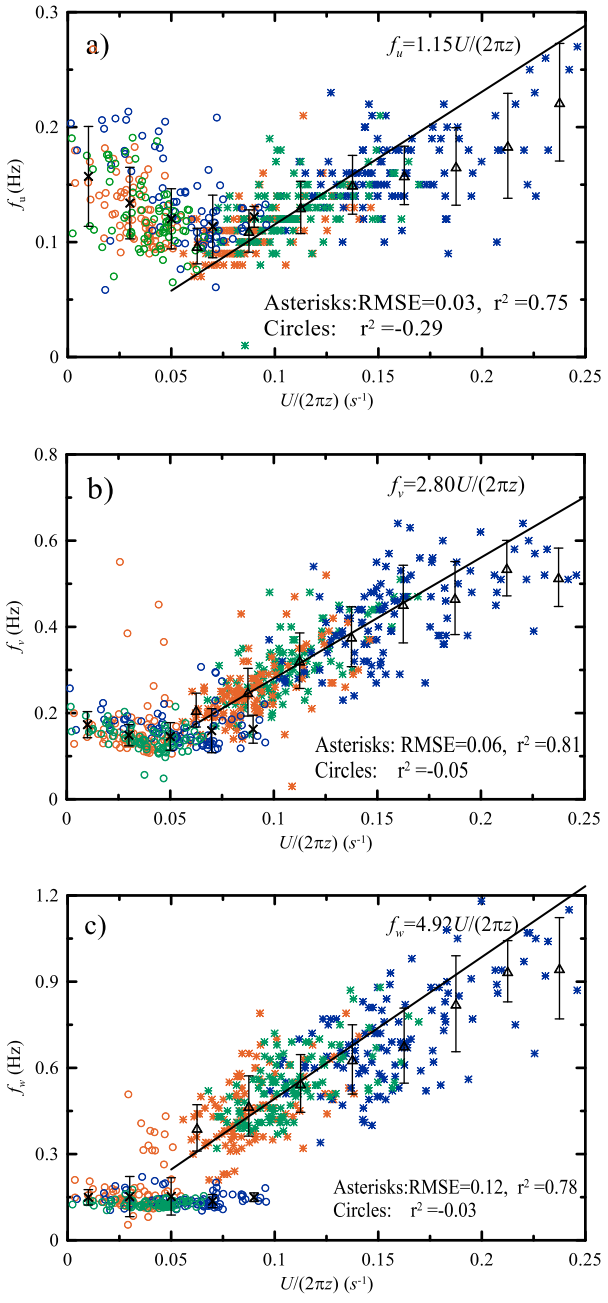

FIG. 5. (a)–(c) Comparison of the longitudinal (f_u), lateral (f_v), and vertical (f_w) intersection frequencies with $U/(2\pi z)$. The asterisks and circles represent the data in which the WC stress accounts for small and large proportions of the total wind stress, respectively. The blue, green, and brown points represent the data at 8.4, 12.4, and 15.3 m above the mean ocean level, respectively. The dark solid lines are $f_i \propto U/(2\pi z)$. The triangles and crosses are the bin-averaged values of the asterisks and circles.

The wind dependence of the normalized intersection frequency (Figs. 6a–c) shows that with an increasing wind speed, the deviation of the observation from $U/(2\pi z)$ becomes small. By fitting the normalized intersection frequency with the wind speed, the following relationships can be found:

$$\frac{U(z)/(2\pi z)}{f_i} = \frac{U(z)^{m_i}}{n_i}. \tag{3.1}$$

The values of m and n for the longitudinal, lateral, and vertical intersections are given in Table 2. For the correlation coefficient and RMSE, they are given in Table 3.

In Figs. 6d–f, a decrease in the deviation from $U/(2\pi z)$ with an increasing WC stress can also be found. Their relationship can be expressed as

$$\frac{U(z)/(2\pi z)}{f_i} = m_i \ln\left(\frac{|\boldsymbol{\tau}_{\text{wave}}|}{\rho_a}\right) + n_i. \tag{3.2}$$

The values of m and n for the longitudinal, lateral, and vertical normalized interactions are 0.17, 0.12, and 0.10 and 1.39, 0.99, and 0.90 (Table 2), respectively.

From the RMSE and correlation coefficients shown in Table 3, it can be seen that although the normalized intersection frequency has a good relationship with the wind speed or WC stress, the three levels of observation do not collapse on the lines given by Eq. (3.1) or Eq. (3.2) (Fig. 6): the normalized interaction frequency at the height of 8 m is slightly larger than that at 12 m, while the values at 12 m are slightly larger than those at 15 m. This indicates other factors can affect the interaction. So this study analyzes the angle difference between wave and wind and atmospheric stability. However, no relationships between them are found (not shown).

To solve this question, we attempted to combine the wind speed and WC stress to analyze their mixed effect according to dimensional analysis: $\{[U(z)/(2\pi z)]/f_i\} \propto |\boldsymbol{\tau}_{\text{wave}}|/(\rho_a U^2) = C_{d\text{wave}}$. Figure 7 shows the ratio changing with the $C_{d\text{wave}}$. Their relationships are as follows:

$$\frac{U(z)/(2\pi z)}{f_i} = p_i C_{d\text{wave}} + q_i. \tag{3.3}$$

The values of p and q for the longitudinal, lateral, and vertical intersections are 902, 614, and 593 and 0.12, 0.12, and 0.12 (Table 2), respectively. The relationship shows that the larger the drag coefficient of the wave effect is, the less the deviation of the intersection frequency from $U/(2\pi z)$.

Compared with parameterizing the normalized intersection frequency with the wind speed or WC stress alone, although the correlation coefficients between the normalized frequency and drag coefficient of the wave effect are lower, they collapse on the solid lines. Additionally, Eq. (3.3) contains the effects of both the wind speed and WC stress. The low relationship may be induced by the different trends in Eqs. (3.1) and (3.2).

b. *Along-wind wave-coherent stress*

The interaction frequency in section 3a shows that it can be affected by the WC stress. However, due to the unclear WC stress magnitude and profile, it is difficult to evaluate the interaction frequency by using Eq. (3.3). Thus, the aim of this section is to derive a function to describe the WC stress.

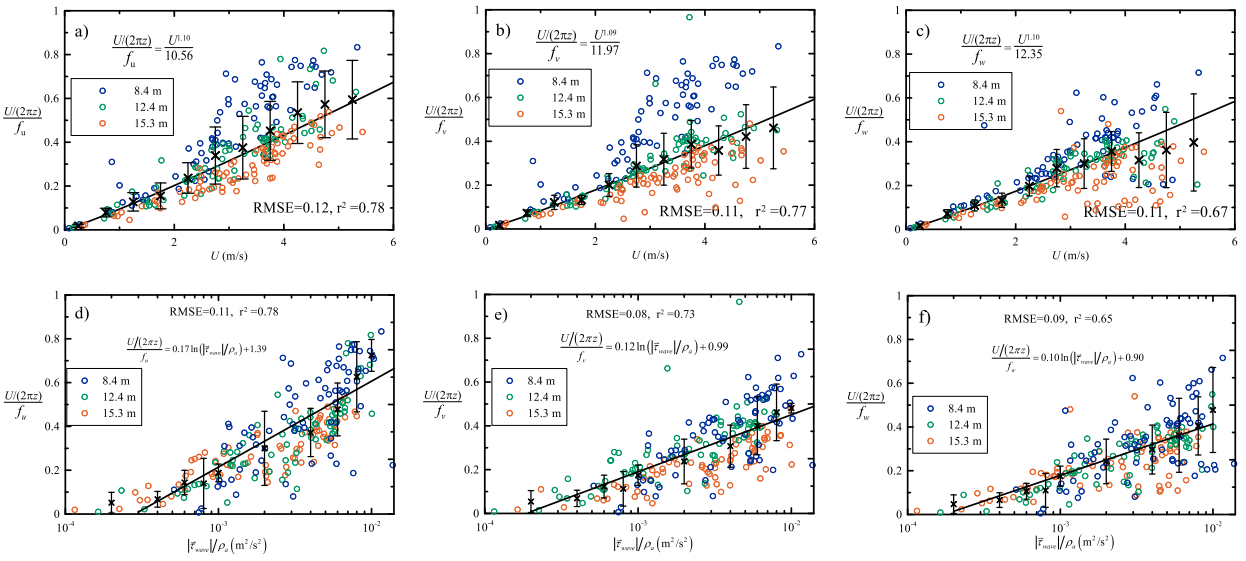

FIG. 6. The ratio of the intersection frequency changing with the wind speed and WC stress. The blue, green, and brown circles represent the data at 8.4, 12.4, and 15.3 m above the mean ocean level, respectively. The crosses are the bin-averaged values. The solid lines are Eqs. (3.1) and (3.2).

The linearized equations used to depict the WC perturbations are as follows:

$$\frac{\partial \tilde{u}}{\partial t} + U\frac{\partial \tilde{u}}{\partial x} + \tilde{w}\frac{\partial U}{\partial z} = -\frac{1}{\rho_a}\frac{\partial \tilde{p}}{\partial x}, \tag{3.4}$$

$$\frac{\partial \tilde{w}}{\partial t} + U\frac{\partial \tilde{w}}{\partial x} = -\frac{1}{\rho_a}\frac{\partial \tilde{p}}{\partial z}. \tag{3.5}$$

Here, $\tilde{u}$ and $\tilde{w}$ are the horizontal and vertical WC perturbations over the surface wave $\tilde{\eta} = -iae^{ik(x-ct)}$, respectively, which are the real parts of $\tilde{u} = -i(\hat{u}_R + i\hat{u}_I)e^{ik(x-ct)}$ and $\tilde{w} = -(\hat{w}_R + i\hat{w}_I)e^{ik(x-ct)}$; U is the wind speed; and $\tilde{p} = \rho_a[-i\alpha + \beta]u_*\omega a e^{ik(x-ct)}$ is the WC pressure. By multiplying Eq. (3.4) by $\tilde{u}$ and multiplying Eq. (3.5) by $\tilde{w}$, we can obtain the kinetic energy budget of coherent wave fluctuations as follows (Hristov and Ruiz-Plancarte 2014):

$$\overline{\tilde{u}\tilde{w}}\frac{\partial U}{\partial z} + \frac{1}{\rho_a}\frac{\partial \overline{\tilde{w}\tilde{p}}}{\partial z} = 0. \tag{3.6}$$

Here, $\partial U/\partial z$ is described by $(\kappa z/u_*)(\partial U/\partial z) = \varphi_m(z/L)$ according to MOST. Within the WBL, our observations showed that the turbulence spectra follow the f^{-1} power law (Fig. 4). As those attached eddies are effective in transporting the flux, it is reasonable to revise MOST as

$$\frac{\kappa z}{u_{*\mathrm{turb}}}\frac{\partial U}{\partial z} = \varphi_m\left(\frac{z}{L_{\mathrm{turb}}}\right), \tag{3.7}$$

where $u_{*\mathrm{turb}}^2 = |\boldsymbol{\tau}_{\mathrm{turb}}/\rho_a|$ and $L_{\mathrm{turb}} = -u_{*\mathrm{turb}}^3\theta_v/g\kappa\overline{w'\theta_v'}$. In this version of the equation, only the turbulences generated by the wind shear and buoyancy force contribute to the wind profile.

At the surface, the imaginary part of $\tilde{w}$ (Im$\tilde{w}$) is 0. By using this boundary condition, we can determine that the real part of the pressure is 0 [Eq. (3.5)]. However, above the surface, this is not true because the imaginary part of $\tilde{w}$ can arise from its interaction with Re$\tilde{w}$ (Cao et al. 2020), leading to a nonzero Re$\tilde{p}$. The simulation of turbulent flow over waves (Yang and Shen 2010; Cao et al. 2020; Cao and Shen 2021) shows that above the viscous layer, the WC pressure decays exponentially with the height as follows: $\tilde{p} = \rho_a(-i\alpha e^{-Akz} + \beta e^{-Bkz})u_*\omega a e^{ik(x-ct)}$. Thus, according to Eq. (3.5), the vertical WC perturbation is $\tilde{w} = -\{[-A\alpha e^{-Akz}/(c-U)] + i[B\beta e^{-Bkz}/(-c+U)]\}u_*\omega a e^{ik(x-ct)}$, and the power of WC pressure is

$$\overline{\tilde{w}\tilde{p}} = \rho_a\frac{a^2}{2}\frac{-B+A}{c-U}u_*^2\omega^2\alpha\beta e^{(-A-B)kz}. \tag{3.8}$$

If we let $(-B+A)\alpha\beta = \gamma$ and $-A-B = -D$, the coherent wave flux in Eq. (3.6) becomes

TABLE 2. The coefficients m and n with 1.96 standard error in Eqs. (3.1)–(3.3) with all data.

	m or p			n or q		
	$i = u$	$i = v$	$i = w$	$i = u$	$i = v$	$i = w$
Eq. (3.1)	1.10 ± 0.07	1.09 ± 0.075	1.10 ± 0.086	10.56 ± 0.89	11.97 ± 1.01	12.35 ± 1.26
Eq. (3.2)	0.17 ± 0.02	0.12 ± 0.015	0.10 ± 0.017	1.39 ± 0.11	0.99 ± 0.088	0.90 ± 0.10
Eq. (3.3)	902 ± 168	614 ± 144	593 ± 134	0.12 ± 0.063	0.12 ± 0.049	0.12 ± 0.045

TABLE 3. The RMSE and correlation coefficient of Eqs. (3.1)–(3.3).

	RMSE			r^2		
	$i = u$	$i = v$	$i = w$	$i = u$	$i = v$	$i = w$
Eq. (3.1)	0.12	0.11	0.11	0.78	0.77	0.67
Eq. (3.2)	0.11	0.08	0.09	0.78	0.73	0.65
Eq. (3.3)	0.15	0.12	0.11	0.54	0.53	0.52

$$\overline{\tilde{u}\tilde{w}} = \int \left[\frac{Dke^{-Dkz}}{(c-U)} - \frac{e^{-Dkz}}{(c-U)^2}\frac{\partial U}{\partial z} \right] \gamma \frac{\kappa z}{u_{*\mathrm{turb}}} u_*^2 \omega^2 S(\omega) d\omega \Big/ \varphi_m\left(\frac{z}{L_{\mathrm{turb}}}\right). \tag{3.9}$$

To determine the coefficients γ and D, we separate the data at each level randomly into two groups: one is used to determine the coefficients γ and D and the other is used to test Eq. (3.9). The coefficients γ and D determined from one group under unstable condition (because MOST has many uncertainties under stable conditions, Baas et al. 2006) are $\gamma = -41.61$ and $D \approx 1.74$. The comparison of the other group of data with Eq. (3.9) is shown in Fig. 8a. It shows good agreement.

Figure 8a shows the integration of the WC stress compared with the observation. One may doubt if Eq. (3.9) coincides with the observation at the peak region. As an example, Fig. 8b shows the cospectra of the along-wind coherent flux computed from Eq. (3.9) compared with the observations. We can see that although the observations swing with changing frequency, the WC flux computed from Eq. (3.9) overlaps with the observation at frequencies between 0.1 and 0.15 Hz (the light orange region). The swing of observation is induced by the difficulty in completely identifying the WC stress from turbulent stress and the random phase shift in Eq. (2.3).

4. Discussion

a. *Regarding Eq. (3.9)*

Measurements in the laboratory (Buckley and Veron 2016) and field experiment (Grare et al. 2018) showed that the vertical WC perturbations reverse signs below and above the critical height due to the abrupt change in the phase shift angle between $\tilde{w}$ and $\tilde{\eta}$. This phenomenon was not anticipated because only the swell cases were selected. At this time, the height where the WC perturbations decay to 0 is lower than the critical height, corresponding to Fig. 7i in Buckley and Veron (2016). Thus, Eq. (3.9) is not suitable for use in wind seas.

To derive Eq. (3.9), the nonlinear terms $\tilde{u}(\partial\tilde{u}/\partial x) + \tilde{w}(\partial\tilde{u}/\partial z)$ in Eq. (3.4) and $\tilde{u}(\partial\tilde{w}/\partial x) + \tilde{w}(\partial\tilde{w}/\partial z)$ in Eq. (3.5) are ignored. If we do not ignore the nonlinear terms, Eq. (3.6) becomes

$$\overline{\tilde{u}\tilde{w}}\frac{\partial U}{\partial z} + \frac{\partial \overline{\tilde{w}\tilde{E}}}{\partial z} + \frac{1}{\rho_a}\frac{\partial \overline{\tilde{p}\tilde{w}}}{\partial z} = 0. \tag{4.1}$$

For a single small-slope wave, even though the third-order interaction ($\overline{\tilde{w}\tilde{E}}$) is usually considered negligible compared with the second-order (Hristov and Ruiz-Plancarte 2014), recent studies (Grare et al. 2013a; Ortiz-Suslow et al. 2021) have indicated that it plays a decisive role in the WC stress. Figure 9a shows an example of our observation. A noteworthy wave-affected region appears in the frequency range from 0.08 to 1.5 Hz (the orange region). These regions are generated when the WC perturbation's wavenumber and frequency satisfy $k_l = k_m \pm k_n$ and $\omega_l = \omega_m \pm \omega_n$. Since the generation of $\overline{\tilde{w}\tilde{E}}$ relies on WC perturbations at high frequency while the WC perturbations at high frequency have lots of uncertainties

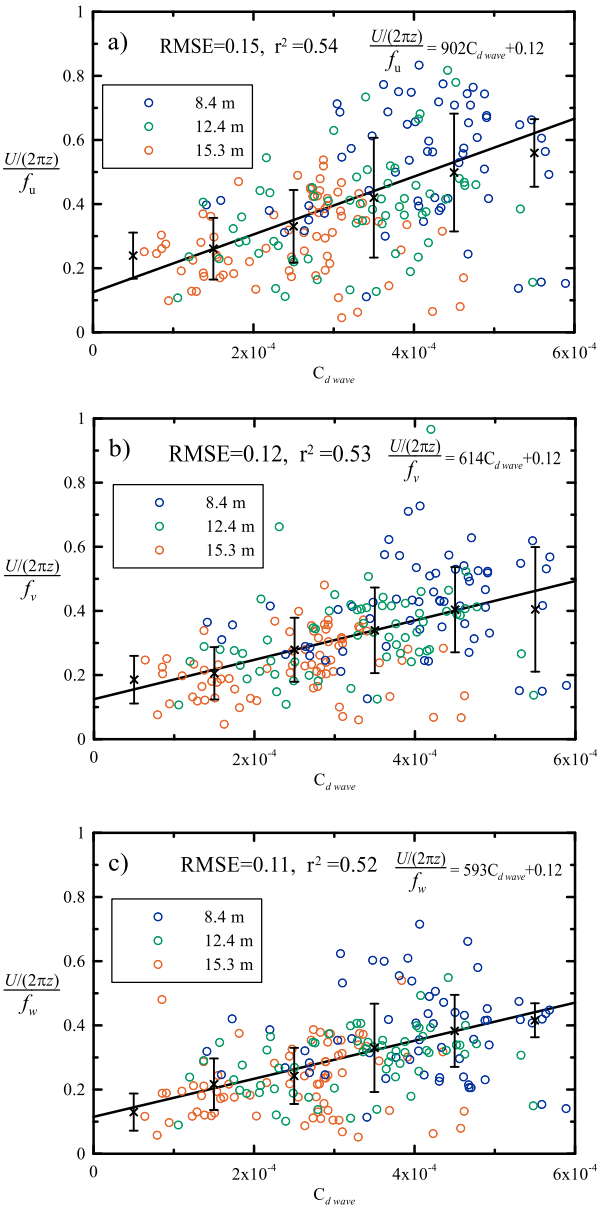

FIG. 7. The relationship between the ratio of the intersection frequency and the drag coefficient of the wave effect $C_{d\mathrm{wave}}$. The blue, green, and brown circles represent the data at 8.4, 12.4, and 15.3 m above the mean ocean level, respectively. The crosses are the bin-averaged values. The solid lines are Eq. (3.3).

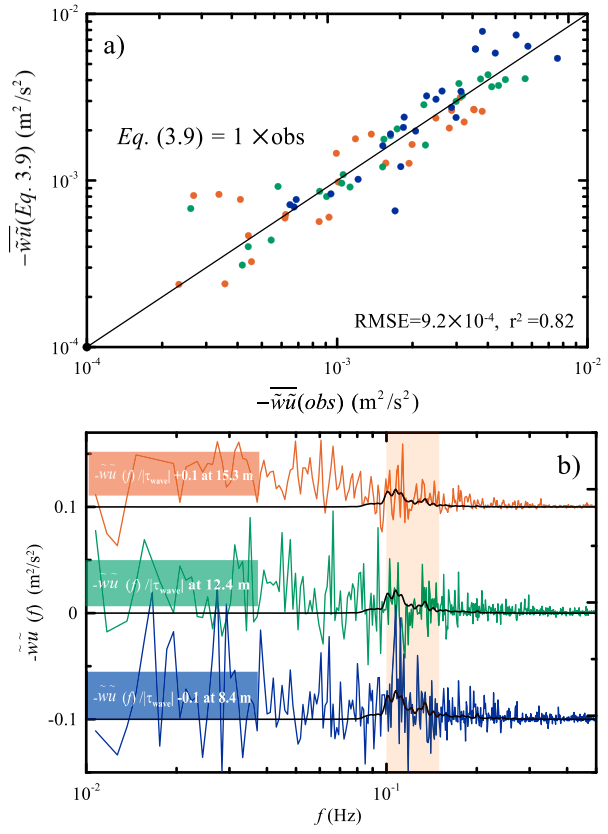

FIG. 8. (a) Comparison of the observed along-wind WC flux with Eq. (3.9). The blue, green, and brown circles are the data at 8.4, 12.4, and 15.3 m above the mean ocean level, respectively. (b) An example of an along-wind WC stress computed from Eq. (3.9) compared with the observation. The same data as those in Figs. 4d and 4f are used. The black solid lines are the results computed from Eq. (3.9).

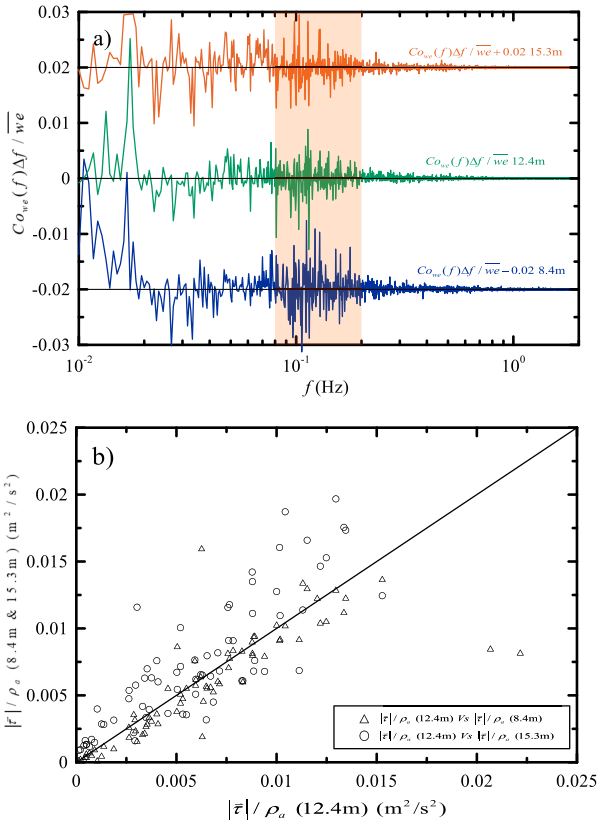

FIG. 9. (a) The cospectra density of $\overline{\tilde{w}\tilde{E}}$ changing with the frequency by using the same data in Figs. 4d–f. The orange shadow shows the wave peak region. (b) Comparison of the three levels of total wind stress.

due to the small amplitudes of those waves, the mechanism is not explored in this study.

Studies by Ortiz-Suslow et al. (2021) have reported that over the ocean, the constant flux layer is rarely available. Mahrt et al. (2018) show that the wind stress decreases with height, while Grare et al. (2013a) show that the wind stress at 10.5 m is slightly larger than that at 7.5 m. This raises another question with regard to whether Eq. (3.7) is appropriate to link the wind gradient with the flux. Figure 9b shows the comparison of the observed momentum flux at three levels. This indicates that the total wind stress does not change significantly with the height. The difference in the total wind stress between two adjacent levels accounts for 4% and 1% of the total wind stress at 12.4 m above the mean ocean level.

Equation (3.9) shows that the WC stress relies on wind speed, wind gradient, total wind stress, and wave spectrum. That is why Fig. 3a has a poor relationship between normalized WC stress with wind speed. To further check the universality of Eq. (3.9), the observation from Zou et al. (2019) is used. During their measurement, the turbulence was observed by an ultrasonic anemometer (Gill R3-50) at 8 m above the mean surface, and the wave was observed by the ADCP [Nortek acoustic Doppler waves and current (AWAC)]. The data are available online (https://www.seanoe.org/data/00506/61732/).

Figure 10 shows the WC flux computed from Eq. (3.9) compared with their observation. Here, only unstable cases were considered. Using $D \approx 1.74$ and $\gamma = -41.61$, Eq. (3.9) shows good agreement with the observation except for being slightly larger than the observation. This comes from the heat flux error because no water vapor is observed to correct the ultrasonic virtual temperature.

b. *The difference between Eq. (3.9) and quasi-linear theory*

The unknown WC stress causes us to use only quasi-linear theory (Janssen 1991) to study the influence of swell on marine ABL:

$$\tau_{\text{wave}} = -\rho_a \overline{\tilde{w}\tilde{u}} = \int_0^\infty \rho_a c_\beta \omega^2 \left(\frac{u_*}{c}\right)^2 S(\omega) d\omega, \tag{4.2}$$

where $c_\beta = 32 \pm 16$ is the wave growth rate coefficient (Plant 1982). To study the influence of swell on marine ABL, current studies (Makin et al. 1995; Hanley and Belcher 2008; Semedo

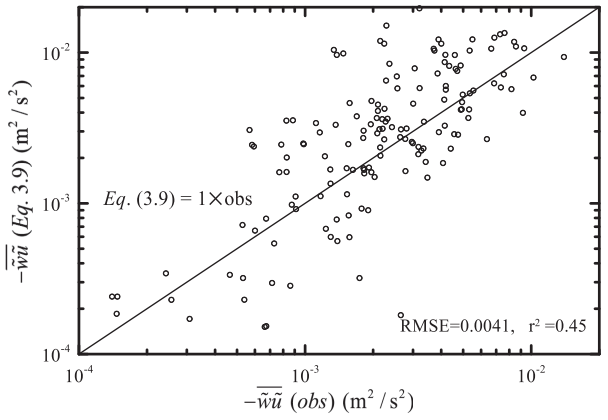

FIG. 10. The observed WC stress was computed from Eq. (3.6) compared with Zou et al. (2019). The solid line is the 1:1 line.

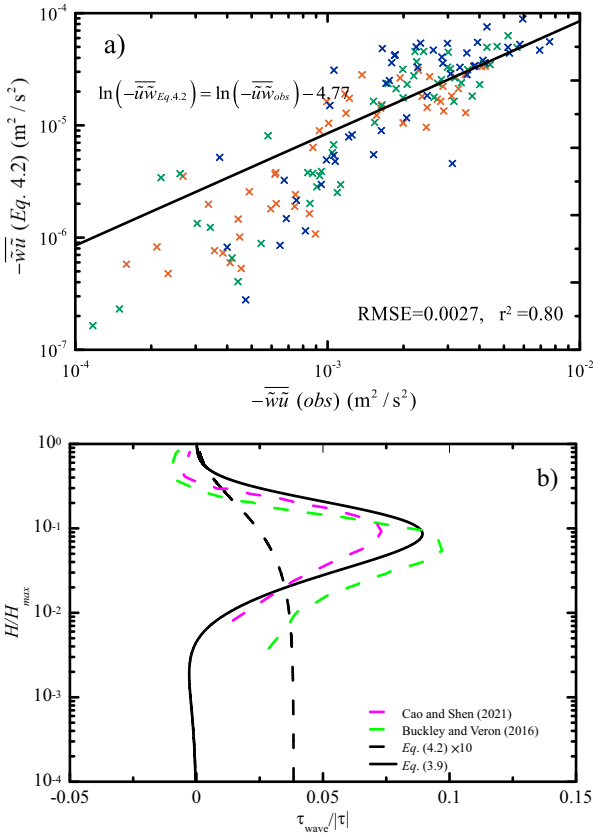

FIG. 11. (a) Comparison of the observed along-wind WC flux with Eq. (4.2). (b) The profile of the WC stress computed from Eq. (3.9) compared with Eq. (4.2). The magenta and green lines are from Cao and Shen (2021)'s Fig. 14 for $c/u_* = 66.67$. The dashed line is from Buckley and Veron's (2016) Fig. 9. They are augmented by a factor of 1/300 and 1/30, respectively.

et al. 2009; Zou et al. 2018; Wu and Qiao 2022) have mostly assumed that Eq. (4.2) decays exponentially with the height: $\tau_{\text{wave}}(0)e^{-Akz}$, where $A = 2$ is the decay coefficient. By combining Eq. (3.6), Cifuentes-Lorenzen et al. (2018) also used the exponential decay of WC stress to investigate the momentum and energy exchange across the WBL.

However, when we compared our observations, we found that this decay format can underestimate the magnitude of the WC stress (Fig. 11a). To explicitly illustrate the difference between Eqs. (3.9) and (4.2), Fig. 11b shows the profile of the WC stress when the local wind blows over the swell wave. Here, the swell wave is simulated by $S(\omega) = S_O(\omega)\exp(-\omega^3/0.1)$, where S_O is the wave spectrum computed from Donelan et al. (1985) by using $U_{10} = 20$ m s^{-1} and a wave age of 0.7. The local wind speed is 7 m s^{-1}. The WC stress is normalized by the total wind stress, and the height is $H/H_{\max}$, where $H = z\omega_p$ and $H_{\max}$ is the height where WC stress decays to 0.

Figure 11b shows that the WC stress computed from Eq. (4.2) decreases with the height, while Eq. (3.9) first increases and then decreases. The first increasing and then decreasing trend of the WC stress is due to the interaction between the power of the WC pressure and the wind gradient. Compared with Eq. (3.9), the feature of Eq. (4.2) is that it gives much smaller values of the WC stress.

To check if the trend of Eq. (3.9) is universal, the magenta and green dashed lines in Fig. 11b show the profiles of the WC stress from Cao and Shen (2021) and Buckley and Veron (2016). Buckley and Veron obtained their profile with laboratory experiments, while Cao and Shen used LES. To clearly show their profile in one figure, the profile of Buckley and Veron (2016) is augmented by a factor of 1/30 while the profile of Cao and Shen (2021) is augmented by a factor of 1/300. It can be seen that the trend of our function is consistent with those of Cao and Shen (2021) and Buckley and Veron (2016).

c. *The wave growth rate of swell*

Equation (4.2) originates from Miles (1957)'s shear instability and the WC stress in shear instability leads to wave growth. Figure 11a shows that Eq. (4.2) gives much smaller values. We can change c_β to make Eq. (4.2) fit the observation accurately. However, this means the swell can grow more rapidly than the wind sea. Different from Eq. (4.2), the WC stress generated by Eq. (3.9) is 0 at the surface (Fig. 11b). One may question how the swell grows.

According to the studies of Snyder et al. (1981), Donelan et al. (2006), and Kahma et al. (2016), the growth of waves is related to the WC pressure rather than the WC stress; thus, the wave growth rate coefficient can be defined as follows:

$$\zeta(f) = \frac{\overline{i\tilde{p}(f)\tilde{\eta}(f)}}{\rho_w g S_{\tilde{\eta}\tilde{\eta}}(f)} = -\frac{\rho_a \beta u_* \omega}{\rho_w g}, \tag{4.3}$$

where β is determined from Eq. (3.5) as follows:

$$\hat{w}_I = -\frac{u_* \omega a B \beta e^{-Bkz}}{c - U}, \tag{4.4}$$

where $\hat{w}_I = \sqrt{S_{\tilde{w}\tilde{w}}}\cos(\theta_{\tilde{\eta}\tilde{w}})$. Equation (4.4) is different from Eq. (17) in Grare et al. (2018) and the function $\tilde{w} \sim (U - c)e^{-kz}$ given by Lighthill (1957), Kudryavtsev et al. (2001), and

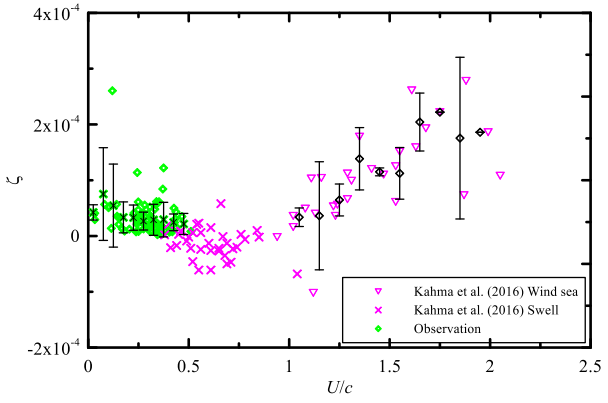

FIG. 12. The wave growth rate vs the inverse wave age. The magenta triangles and crosses represent the results of Kahma et al. (2016) under swell conditions and wind-sea conditions, respectively. The green diamonds are our observations. The black crosses and diamonds are the bin-averaged values.

Kudryavtsev and Makin (2004). We also emphasized that the actual WC perturbation profile may not be so simple because not only the height but also wind speed or wind gradient could affect the WC pressure.

By using three levels of observations, we derived the exponential coefficient β and then computed the wave growth rate. Figure 12 shows the wave growth rate changing with inverse wave age. The result from Kahma et al. (2016) is also added for comparison. It can be seen that our observation is very scattered. Compared with Kahma et al. (2016) under the wind sea, the bin average of our observation does not have a strong relationship with the inverse wave age. Their correlation coefficient is −0.14.

5. Conclusions

Understanding the physical mechanism of the interaction between ocean surface waves and wind has been a long-standing challenge due to the complicated processes occurring in the lower part of the marine ABL. In this study, the WC stress and the turbulent structure under the modulation of surface waves are studied by using three levels of observations.

The attached eddy model (AEM) predicts that the intersection between the energy-containing and inertial dissipation ranges follows $\sim U/(2\pi z)$. Our observation showed good agreement with the model when WC stress accounted for a small proportion of the total wind stress (Fig. 4). Additionally, the results show that the length of the vertical plateau decreases with a decreasing height. This may be due to the dampening effect of the surface.

The effect of the WC perturbation on the turbulent structure when the WC stress accounts for a large part of the total wind stress was studied. The results show that the intersection frequency is higher than that predicted by the AEM and that both the wind speed and WC pressure can affect the intersection frequency. Their effects were parameterized based on the drag coefficient of the wave-coherent flux.

Within the WBL, where the total stress can be separated into turbulent stress and WC stress, the unclear magnitude and profile of the WC stress exerted by swell make it difficult to evaluate the intersection frequency. After considering the interaction of surface waves and wind gradients, a new relationship that describes the WC stress is derived in this study.

Acknowledgments. This work was supported by the National Natural Science Foundation of China (42276001 and 41830533) and the National Key Research and Development Program of China (2023YFC3008004).

Data availability statement. The raw data are owned by Prof. Qiao at the First Institute of Oceanography, Ministry of Natural Resources. All data needed to evaluate the conclusion in the paper are available at https://doi.org/10.17882/100650 and https://www.seanoe.org/data/00506/61732/.

REFERENCES

Baas, P., G. J. Steeneveld, B. J. H. van de Wiel, and A. A. M. Holtslag, 2006: Exploring self-correlation in flux–gradient relationships for stably stratified conditions. *J. Atmos. Sci.*, **63**, 3045–3054, https://doi.org/10.1175/JAS3778.1.

Babanin, A. V., J. McConochie, and D. Chalikov, 2018: Winds near the surface of waves: Observations and modeling. *J. Phys. Oceanogr.*, **48**, 1079–1088, https://doi.org/10.1175/JPO-D-17-0009.1.

Buckley, M. P., and F. Veron, 2016: Structure of the airflow above surface waves. *J. Phys. Oceanogr.*, **46**, 1377–1397, https://doi.org/10.1175/JPO-D-15-0135.1.

Cao, T., and L. Shen, 2021: A numerical and theoretical study of wind over fast-propagating water waves. *J. Fluid Mech.*, **919**, A38, https://doi.org/10.1017/jfm.2021.416.

——, B.-Q. Deng, and L. Shen, 2020: A simulation-based mechanistic study of turbulent wind blowing over opposing water waves. *J. Fluid Mech.*, **901**, A27, https://doi.org/10.1017/jfm.2020.591.

Chalikov, D., 1995: The parameterization of the wave boundary layer. *J. Phys. Oceanogr.*, **25**, 1333–1349, https://doi.org/10.1175/1520-0485(1995)025<1333:TPOTWB>2.0.CO;2.

Chalikov, D. V., and V. K. Makin, 1991: Models of the wave boundary layer. *Bound.-Layer Meteor.*, **56**, 83–99, https://doi.org/10.1007/BF00119963.

Chen, S., F. Qiao, J. A. Zhang, H. Ma, Y. Xue, and S. Chen, 2020: Swell modulation on wind stress in the constant flux layer. *Geophys. Res. Lett.*, **47**, e2020GL089883, https://doi.org/10.1029/2020GL089883.

Cifuentes-Lorenzen, A., J. B. Edson, and C. J. Zappa, 2018: Air–sea interaction in the Southern Ocean: Exploring the height of the wave boundary layer at the air–sea interface. *Bound.-Layer Meteor.*, **169**, 461–482, https://doi.org/10.1007/s10546-018-0376-0.

Del Álamo, J. C., and J. Jiménez, 2009: Estimation of turbulent convection velocities and corrections to Taylor's approximation. *J. Fluid Mech.*, **640**, 5–26, https://doi.org/10.1017/S0022112009991029.

Donelan, M. A., J. Hamilton, W. H. Hui, and R. W. Stewart, 1985: Directional spectra of wind-generated ocean waves. *Philos. Trans. Roy. Soc.*, **A315**, 509–562, https://doi.org/10.1098/rsta.1985.0054.

——, W. M. Drennan, and K. B. Katsaros, 1997: The air–sea momentum flux in conditions of wind sea and swell. *J. Phys.*

Oceanogr., **27**, 2087–2099, https://doi.org/10.1175/1520-0485(1997)027<2087:TASMFI>2.0.CO;2.

——, A. V. Babanin, I. R. Young, and M. L. Banner, 2006: Wave-follower field measurements of the wind-input spectral function. Part II: Parameterization of the wind input. *J. Phys. Oceanogr.*, **36**, 1672–1689, https://doi.org/10.1175/JPO2933.1.

Drobinski, P., P. Carlotti, R. K. Newsom, R. M. Banta, R. C. Foster, and J.-L. Redelsperger, 2004: The structure of the near-neutral atmospheric surface layer. *J. Atmos. Sci.*, **61**, 699–714, https://doi.org/10.1175/1520-0469(2004)061<0699:TSOTNA>2.0.CO;2.

——, ——, J.-L. Redelsperger, V. Masson, R. M. Banta, and R. K. Newsom, 2007: Numerical and experimental investigation of the neutral atmospheric surface layer. *J. Atmos. Sci.*, **64**, 137–156, https://doi.org/10.1175/JAS3831.1.

Ghannam, K., G. G. Katul, E. Bou-Zeid, T. Gerken, and M. Chamecki, 2018: Scaling and similarity of the anisotropic coherent eddies in near-surface atmospheric turbulence. *J. Atmos. Sci.*, **75**, 943–964, https://doi.org/10.1175/JAS-D-17-0246.1.

Grachev, A. A., and C. W. Fairall, 2001: Upward momentum transfer in the marine boundary layer. *J. Phys. Oceanogr.*, **31**, 1698–1711, https://doi.org/10.1175/1520-0485(2001)031<1698:UMTITM>2.0.CO;2.

——, ——, J. E. Hare, J. B. Edson, and S. D. Miller, 2003: Wind stress vector over ocean waves. *J. Phys. Oceanogr.*, **33**, 2408–2429, https://doi.org/10.1175/1520-0485(2003)033<2408:WSVOOW>2.0.CO;2.

Grare, L., L. Lenain, and W. K. Melville, 2013a: Wave-coherent airflow and critical layers over ocean waves. *J. Phys. Oceanogr.*, **43**, 2156–2172, https://doi.org/10.1175/JPO-D-13-056.1.

——, W. L. Peirson, J. W. Walker, H. Branger, J.-P. Giovanangeli, and V. Makin, 2013b: Growth and dissipation of wind-forced, deep-water waves. *J. Fluid Mech.*, **722**, 5–50, https://doi.org/10.1017/jfm.2013.88.

——, L. Lenain, and W. K. Melville, 2018: Vertical profiles of the wave-induced airflow above ocean surface waves. *J. Phys. Oceanogr.*, **48**, 2901–2922, https://doi.org/10.1175/JPO-D-18-0121.1.

Hanley, K. E., and S. E. Belcher, 2008: Wave-driven wind jets in the marine atmospheric boundary layer. *J. Atmos. Sci.*, **65**, 2646–2660, https://doi.org/10.1175/2007JAS2562.1.

Hanson, J. L., and R. E. Jensen, 2004: Wave system diagnostics for numerical wave models. *Eighth Int. Workshop on Wave Hindcasting and Forecasting*, Oahu, HI, WMO/IOC Joint Technical Commission for Oceanography and Marine Meteorology, 231–238.

Hao, X., and L. Shen, 2022: Large-eddy simulation of gusty wind turbulence over a travelling wave. *J. Fluid Mech.*, **946**, A8, https://doi.org/10.1017/jfm.2022.577.

Harris, D. L., 1966: The wave-driven wind. *J. Atmos. Sci.*, **23**, 688–693, https://doi.org/10.1175/1520-0469(1966)023<0688:TWDW>2.0.CO;2.

Högström, U., J. C. R. Hunt, and A.-S. Smedman, 2002: Theory and measurements for turbulence spectra and variances in the atmospheric neutral surface layer. *Bound.-Layer Meteor.*, **103**, 101–124, https://doi.org/10.1023/A:1014579828712.

——, E. Sahlée, A.-S. Smedman, A. Rutgersson, E. Nilsson, K. K. Kahma, and W. M. Drennan, 2015: Surface stress over the ocean in swell-dominated conditions during moderate winds. *J. Atmos. Sci.*, **72**, 4777–4795, https://doi.org/10.1175/JAS-D-15-0139.1.

Hristov, T., and J. Ruiz-Plancarte, 2014: Dynamic balances in a wavy boundary layer. *J. Phys. Oceanogr.*, **44**, 3185–3194, https://doi.org/10.1175/JPO-D-13-0209.1.

Huang, J., and Coauthors, 2021: The turbulent structure of the marine atmospheric boundary layer during and before a cold front. *J. Atmos. Sci.*, **78**, 863–875, https://doi.org/10.1175/JAS-D-19-0314.1.

Hunt, J. C. R., and J. F. Morrison, 2000: Eddy structure in turbulent boundary layers. *Eur. J. Mech.*, **19B**, 673–694, https://doi.org/10.1016/S0997-7546(00)00129-1.

——, and P. Carlotti, 2001: Statistical structure at the wall of the high Reynolds number turbulent boundary layer. *Flow, Turbul. Combust.*, **66**, 453–475, https://doi.org/10.1023/A:1013519021030.

Hutchins, N., K. Chauhan, I. Marusic, J. Monty, and J. Klewicki, 2012: Towards reconciling the large-scale structure of turbulent boundary layers in the atmosphere and laboratory. *Bound.-Layer Meteor.*, **145**, 273–306, https://doi.org/10.1007/s10546-012-9735-4.

Janssen, P., 2004: *The Interaction of Ocean Waves and Wind*. Cambridge University Press, 308 pp., https://doi.org/10.1017/CBO9780511525018.

Janssen, P. A. E. M., 1991: Quasi-linear theory of wind-wave generation applied to wave forecasting. *J. Phys. Oceanogr.*, **21**, 1631–1642, https://doi.org/10.1175/1520-0485(1991)021<1631:QLTOWW>2.0.CO;2.

——, and P. Viterbo, 1996: Ocean waves and the atmospheric climate. *J. Climate*, **9**, 1269–1287, https://doi.org/10.1175/1520-0442(1996)009<1269:OWATAC>2.0.CO;2.

Jeffreys, H. S., 1925: On the formation of water waves by wind. *Proc. Roy. Soc. London*, **107A**, 189–206, https://doi.org/10.1098/rspa.1925.0015.

Jiang, Q., P. Sullivan, S. Wang, J. Doyle, and L. Vincent, 2016: Impact of swell on air–sea momentum flux and marine boundary layer under low-wind conditions. *J. Atmos. Sci.*, **73**, 2683–2697, https://doi.org/10.1175/JAS-D-15-0200.1.

Kahma, K. K., M. A. Donelan, W. M. Drennan, and E. A. Terray, 2016: Evidence of energy and momentum flux from swell to wind. *J. Phys. Oceanogr.*, **46**, 2143–2156, https://doi.org/10.1175/JPO-D-15-0213.1.

Katul, G., and C.-R. Chu, 1998: A theoretical and experimental investigation of energy-containing scales in the dynamic sublayer of boundary-layer flows. *Bound.-Layer Meteor.*, **86**, 279–312, https://doi.org/10.1023/A:1000657014845.

Katul, G. G., A. Porporato, and V. Nikora, 2012: Existence of k^{-1} power-law scaling in the equilibrium regions of wall-bounded turbulence explained by Heisenberg's eddy viscosity. *Phys. Rev.*, **86E**, 066311, https://doi.org/10.1103/PhysRevE.86.066311.

Kihara, N., H. Hanazaki, T. Mizuya, and H. Ueda, 2007: Relationship between airflow at the critical height and momentum transfer to the traveling waves. *Phys. Fluids*, **19**, 015102, https://doi.org/10.1063/1.2409736.

Kudryavtsev, V. N., and V. K. Makin, 2004: Impact of swell on the marine atmospheric boundary layer. *J. Phys. Oceanogr.*, **34**, 934–949, https://doi.org/10.1175/1520-0485(2004)034<0934:IOSOTM>2.0.CO;2.

——, ——, and J. F. Meirink, 2001: Simplified model of the air flow above waves. *Bound.-Layer Meteor.*, **100**, 63–90, https://doi.org/10.1023/A:1018914113697.

Kunkel, G. J., and I. Marusic, 2006: Study of the near-wall-turbulent region of the high-Reynolds-number boundary layer using an atmospheric flow. *J. Fluid Mech.*, **548**, 375–402, https://doi.org/10.1017/S0022112005007780.

Lighthill, M. J., 1957: The fundamental solution for small steady three-dimensional disturbances to a two-dimensional parallel

shear flow. *J. Fluid Mech.*, **3**, 113–144, https://doi.org/10.1017/S002211205700052X.

Liu, C., X. Li, J. Song, Z. Zou, J. Huang, J. A. Zhang, G. Jie, and J. Wang, 2022: Characteristics of the marine atmospheric boundary layer under the influence of ocean surface waves. *J. Phys. Oceanogr.*, **52**, 1261–1276, https://doi.org/10.1175/JPO-D-21-0164.1.

Mahrt, L., S. Miller, T. Hristov, and J. Edson, 2018: On estimating the surface wind stress over the sea. *J. Phys. Oceanogr.*, **48**, 1533–1541, https://doi.org/10.1175/JPO-D-17-0267.1.

Makin, V. K., V. N. Kudryavtsev, and C. Mastenbroek, 1995: Drag of the sea surface. *Bound.-Layer Meteor.*, **73**, 159–182, https://doi.org/10.1007/BF00708935.

Marušić, I., and A. E. Perry, 1995: A wall-wake model for the turbulence structure of boundary layers. Part 2. Further experimental support. *J. Fluid Mech.*, **298**, 389–407, https://doi.org/10.1017/S0022112095003363.

Miles, J. W., 1957: On the generation of surface waves by shear flows. *J. Fluid Mech.*, **3**, 185–204, https://doi.org/10.1017/S0022112057000567.

Ortiz-Suslow, D. G., Q. Wang, J. Kalogiros, and R. Yamaguchi, 2020: A method for identifying Kolmogorov's inertial subrange in the velocity variance spectrum. *J. Atmos. Oceanic Technol.*, **37**, 85–102, https://doi.org/10.1175/JTECH-D-19-0028.1.

——, J. Kalogiros, R. Yamaguchi, and Q. Wang, 2021: An evaluation of the constant flux layer in the atmospheric flow above the wavy air-sea interface. *J. Geophys. Res. Atmos.*, **126**, e2020JD032834, https://doi.org/10.1029/2020JD032834.

Pan, Y., and M. Chamecki, 2016: A scaling law for the shear-production range of second-order structure functions. *J. Fluid Mech.*, **801**, 459–474, https://doi.org/10.1017/jfm.2016.427.

Perry, A. E., and M. S. Chong, 1982: On the mechanism of wall turbulence. *J. Fluid Mech.*, **119**, 173–217, https://doi.org/10.1017/S0022112082001311.

——, and I. Marušić, 1995: A wall-wake model for the turbulence structure of boundary layers. Part 1. Extension of the attached eddy hypothesis. *J. Fluid Mech.*, **298**, 361–388, https://doi.org/10.1017/S0022112095003351.

——, S. Henbest, and M. S. Chong, 1986: A theoretical and experimental study of wall turbulence. *J. Fluid Mech.*, **165**, 163–199, https://doi.org/10.1017/S002211208600304X.

Phillips, O. M., 1957: On the generation of waves by turbulent wind. *J. Fluid Mech.*, **2**, 417–445, https://doi.org/10.1017/S0022112057000233.

Plant, W. J., 1982: A relationship between wind stress and wave slope. *J. Geophys. Res.*, **87**, 1961–1967, https://doi.org/10.1029/JC087iC03p01961.

Rieder, K. F., and J. A. Smith, 1998: Removing wave effects from the wind stress vector. *J. Geophys. Res.*, **103**, 1363–1374, https://doi.org/10.1029/97JC02571.

Rutgersson, A., A.-S. Smedman, and U. Högström, 2001: Use of conventional stability parameters during swell. *J. Geophys. Res.*, **106**, 27 117–27 134, https://doi.org/10.1029/2000jc000543.

——, E. O. Nilsson, and R. Kumar, 2012: Introducing surface waves in a coupled wave-atmosphere regional climate model: Impact on atmospheric mixing length. *J. Geophys. Res.*, **117**, C00J15, https://doi.org/10.1029/2012JC007940.

Semedo, A., Ø. Saetra, A. Rutgersson, K. K. Kahma, and H. Pettersson, 2009: Wave-induced wind in the marine boundary layer. *J. Atmos. Sci.*, **66**, 2256–2271, https://doi.org/10.1175/2009JAS3018.1.

Smedman, A., U. Högström, E. Sahleé, W. M. Drennan, K. K. Kahma, H. Pettersson, and F. Zhang, 2009: Observational study of marine atmospheric boundary layer characteristics during swell. *J. Atmos. Sci.*, **66**, 2747–2763, https://doi.org/10.1175/2009JAS2952.1.

Snyder, R. L., F. W. Dobson, J. A. Elliott, and R. B. Long, 1981: Array measurements of atmospheric pressure fluctuations above surface gravity waves. *J. Fluid Mech.*, **102**, 1–59, https://doi.org/10.1017/S0022112081002528.

Song, J., W. Fan, S. Li, and M. Zhou, 2015: Impact of surface waves on the steady near-surface wind profiles over the ocean. *Bound.-Layer Meteor.*, **155**, 111–127, https://doi.org/10.1007/s10546-014-9983-6.

Sullivan, P. P., J. C. McWilliams, and C.-H. Moeng, 2000: Simulation of turbulent flow over idealized water waves. *J. Fluid Mech.*, **404**, 47–85, https://doi.org/10.1017/S0022112099006965.

——, J. B. Edson, T. Hristov, and J. C. McWilliams, 2008: Large-eddy simulations and observations of atmospheric marine boundary layers above nonequilibrium surface waves. *J. Atmos. Sci.*, **65**, 1225–1245, https://doi.org/10.1175/2007JAS2427.1.

——, J. C. McWilliams, and E. G. Patton, 2014: Large-eddy simulation of marine atmospheric boundary layers above a spectrum of moving waves. *J. Atmos. Sci.*, **71**, 4001–4027, https://doi.org/10.1175/JAS-D-14-0095.1.

Taylor, G. I., 1938: The spectrum of turbulence. *Proc. Roy. Soc. London*, **164A**, 476–490, https://doi.org/doi:10.1098/rspa.1938.0032.

Toffoli, A., A. Babanin, M. Onorato, and T. Waseda, 2010: Maximum steepness of oceanic waves: Field and laboratory experiments. *Geophys. Res. Lett.*, **37**, L05603, https://doi.org/10.1029/2009GL041771.

Townsend, A. A. R., 1976: *The Structure of Turbulent Shear Flow*. Cambridge University Press, 429 pp.

Vickers, D., and L. Mahrt, 2003: The cospectral gap and turbulent flux calculations. *J. Atmos. Oceanic Technol.*, **20**, 660–672, https://doi.org/10.1175/1520-0426(2003)20<660:TCGATF>2.0.CO;2.

Wang, L.-H., C.-X. Xu, H. J. Sung, and W.-X. Huang, 2021a: Wall-attached structures over a traveling wavy boundary: Turbulent velocity fluctuations. *Phys. Rev. Fluids*, **6**, 034611, https://doi.org/10.1103/PhysRevFluids.6.034611.

Wang, W., C. Pan, and J. Wang, 2021b: Energy transfer structures associated with large-scale motions in a turbulent boundary layer. *J. Fluid Mech.*, **906**, A14, https://doi.org/10.1017/jfm.2020.777.

Wu, L., and F. Qiao, 2022: Wind profile in the wave boundary layer and its application in a coupled atmosphere-wave model. *J. Geophys. Res. Oceans*, **127**, e2021JC018123, https://doi.org/10.1029/2021JC018123.

Yang, D., and L. Shen, 2010: Direct-simulation-based study of turbulent flow over various waving boundaries. *J. Fluid Mech.*, **650**, 131–180, https://doi.org/10.1017/S0022112009993557.

Zou, Z., D. Zhao, B. Liu, J. A. Zhang, and J. Huang, 2017: Observation-based parameterization of air-sea fluxes in terms of wind speed and atmospheric stability under low-to-moderate wind conditions. *J. Geophys. Res. Oceans*, **122**, 4123–4142, https://doi.org/10.1002/2016JC012399.

——, ——, J. A. Zhang, S. Li, Y. Cheng, H. Lv, and X. Ma, 2018: The influence of swell on the atmospheric boundary layer under nonneutral conditions. *J. Phys. Oceanogr.*, **48**, 925–936, https://doi.org/10.1175/JPO-D-17-0195.1.

——, J. Song, P. Li, J. Huang, J. A. Zhang, Z. Wan, and S. Li, 2019: Effects of swell waves on atmospheric boundary layer turbulence: A low wind field study. *J. Geophys. Res. Oceans*, **124**, 5671–5685, https://doi.org/10.1029/2019JC015153.